Citation
Liu, Y. and Paskevicius, M. and Sofianos, M.V. and Parkinson, G. and Li, C.Z. 2021. In situ SAXS studies of the pore development in biochar during gasification. Carbon. 172: pp. 454-462. http://doi.org/10.1016/j.carbon.2020.10.028

In situ SAXS studies of the pore development in biochar during gasification

Yurong Liu[1], Mark Paskevicius[1], M. Veronica Sofianos[1,2], Gordon Parkinson[1], Chun-Zhu Li[1*]

[1] *Fuels and Energy Technology Institute, Curtin University, GPO Box U1987, Perth, WA 6845, Australia*

[2] *School of Chemical and Bioprocess Engineering, University College Dublin, Belfield, Dublin 4, Ireland*

Abstract

This work investigates the pore development in biochar during gasification using synchrotron small angle X-ray scattering (SAXS) as an *in situ* characterization technique. The influence of the gasifying agents (H_2O, CO_2 or H_2O/CO_2) and temperature on the pore structure development in biochar was studied by carrying out the hour-long gasification of mallee wood biochar (106–250 µm) in: (i) H_2O at 700, 800 and 900°C respectively, (ii) CO_2 at 700 and 800°C, and (iii) a mixture of H_2O and CO_2 (H_2O/CO_2) at 800°C. There was a minor increase in the micro- and mesopore volumes in biochar during gasification in H_2O at 700°C, in contrast to CO_2 gasification at the same temperature where no measurable changes to the pore structure were observed. At 800°C, biochar derived from H_2O/CO_2 gasification exhibited the highest specific surface area (SSA). CO_2 tended to produce a highly microporous biochar with a mesopore network showing pore fractal features. Micropore enlargement was a major process in the presence of H_2O. In this case, the pore structure evolved from being a porous network of branched micropore clusters (pore fractal) to being dominated by rough surfaced mesopores (surface fractal) during gasification in H_2O and H_2O/CO_2. The evolution of pore structures result from the different ways in which carbon atoms were removed by either H_2O or CO_2. H_2O is more reactive and less selective towards reacting with biochar, resulting in a less worm-like network of pores than CO_2. Moreover, it was found that increasing

temperatures can lead to faster rates of pore generation and pore enlargement, which is attributed to the increased reaction rate and the less selective removal of carbon atoms.

Keywords: *in situ*, SAXS, pore development, selective carbon removal, surface fractal, pore fractal, specific surface area, pore volume, biochar gasification.

1. Introduction

Biomass, as a widely available and carbon neutral resource, plays an important role in supplying clean and affordable energy. Gasification is a highly efficient technology to utilize biomass for power generation, as well as for the production of biofuels and chemicals [1]. Biomass gasification is a thermo-chemical process to convert biomass to syngas and biochar [2]. During gasification, biochar reacts with the gasifying agents and undergoes drastic changes in both its chemical and physical structure [3,4]. The study of pore evolution in biochar during gasification is critical to understanding the gasification process, as well as to optimizing the conditions that are used for the preparation of activated carbon using biochar as a precursor [5–8].

It has been reported [9–12] that the pore structure of biochar largely depends on the gasification conditions such as the biomass feedstocks, the gasifying agents and the carbon conversion level. Particularly, the pore structure of biochar from H_2O (steam) gasification has been found to be different from that of biochar obtained from CO_2 gasification [5,10,11,13]. However, different results have been obtained regarding the effects of steam and CO_2 on the porosity development in biochar. Some studies found the maximum micropore development in biochar when subjected to steam gasification [10,14], while others reported that CO_2

gasification resulted in the maximum level of microporosity [6,13,15,16]. Additionally, it has not reached an agreement regarding whether there is a synergistic, competitive or additive effect between H_2O and CO_2 during gasification in the mixture of H_2O and CO_2.

Those reported results are based on measurements using a wide range of techniques including N_2 adsorption (BET), scanning and transmission electron microscopy (SEM and TEM), as well as SAXS and small angle neutron scattering (SANS). Among these techniques, SAXS has been historically utilized to characterize the porosity and the pore morphology of coal and porous carbon with the advantage of detecting both closed and open pores over wide dimension ranges [11,17–23]. Moreover, SAXS can provide the textural properties (e.g. surface roughness or aggregation) of biochar by giving fractal information of the pore network [24–27]. The development of the pore network reflects the evolution of the carbon matrix during gasification, which depends on the reaction pathways of gasification. Therefore, the evolution in the porous network of biochar is of great importance for understanding the reaction pathways during gasification. However, little has been reported on the evolution of the porous network of biochar along gasification. Moreover, *in situ* SAXS is capable of tracking the real-time changes of pore structure under high temperatures throughout the process of gasification. In this way, the *in situ* SAXS measurement avoids the possible changes in biochar structure during cooling down, which can be a shortcoming of *ex situ* measurements. To the best of our knowledge, no *in situ* SAXS measurements of this kind have been previously performed.

To this end, this study uses synchrotron SAXS to characterize the real-time evolution of the pore structure of biochar during gasification. Gasifying agents including H_2O, CO_2 and their mixture were used with the aim of studying the effects of different gasifying agents on

the pore development of biochar. The influence of gasification temperature (700, 800 and 900°C) on the development of pores in biochar was also investigated.

2. Experimental

2.1. *In situ* SAXS measurement

In situ SAXS measurements were conducted at the SAXS beamline of the Australian Synchrotron, Melbourne, Australia [28]. The X-ray beam energy and size was 20 keV and 240 (horizontally) X 24 (vertically) µm respectively. Data were acquired using a Pilatus 1 M detector at a camera length of 959 mm, which corresponds to a q-range of 0.03-1.5 $Å^{-1}$ (q is the scattering vector $q = (4\pi/\lambda)\sin(\theta/2)$, λ (0.62 Å) and θ are the wavelength and scattering angle) [29]. The q range approximately corresponds to observing a pore diameter ranging from 4 to 180 Å [29]. The SAXS patterns were acquired every 1 s during gasification. Silver behenate was used to calibrate the q-scale of the instrument, and a 1 mm thick glassy carbon standard was used for absolute intensity calibration [30]. The background scattering from the capillary was subtracted using a single measurement of an empty capillary.

2.2. Experimental set-up

The biochar (106-250 µm) used in this study is from the pyrolysis and gasification of mallee wood in Renergi's gasification demonstration plant at Curtin University, Australia [31,32]. The biochar precursor was loaded into a thin-walled quartz capillary (OD = 1 mm, wall thickness is 0.01 mm) open at both ends. Quartz wool was firmly inserted at both sides of the biochar to prevent sample displacement while allowing gas flow through the samples (Fig. 1). A total of 3 different gasifying gases including steam (3 vol. % H_2O in argon), pure CO_2 and a mixture of steam and CO_2 (3 vol. % H_2O in CO_2) were used in this study. Steam was generated by flowing argon or CO_2 through 2 connected gas washing bottles that contained DI water (a

100% relative humidity at room temperature gives a ~3 vol. % steam at 800-900 °C). Gas was flowed through the sample from one end to another of the capillary with a flow rate of 10 ml min^{-1} controlled by a mass flow controller (Alicat MC).

Biochar samples were heated to operating temperature under an argon flow before switching to the prescribed gasifying agent. During this process, SAXS data were collected for 60 min or until the biochar was fully consumed. It should also be mentioned that one data set was collected during the heating of biochar up to 900°C in pure argon, where no changes in the scattering intensities were observed to verify that the pore network does not change under these conditions. The heating of biochar was achieved by placing a hot-air blower underneath the capillary, which can provide a uniform heating of the sample in the X-ray beam. A K-type thermocouple was placed on the outside of the capillary and fixed next to the sample in the beam to accurately measure the temperature. All the experiments were operated under ambient pressure.

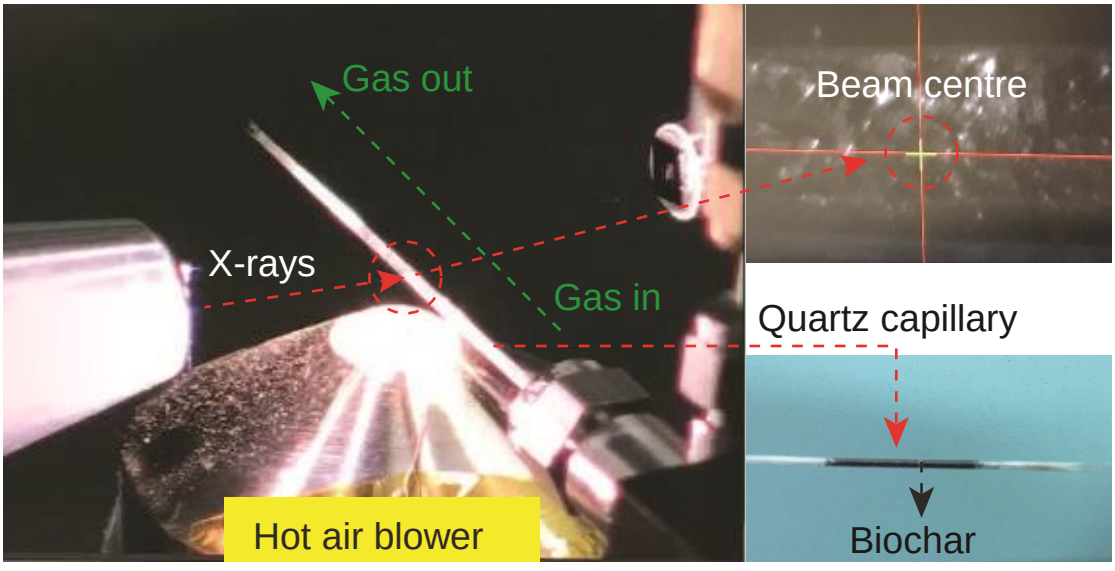

Fig. 1. Diagram showing the experimental set-up in place on the SAXS beamline at the Australian Synchrotron.

2.3. Data processing

The collected SAXS patterns were background subtracted using Scatterbrain [33,34] before being converted to an absolute scale by normalising the intensity by the sample thickness with reference to a known glassy carbon standard [35]. The solid thickness of the sample was calculated using Eq. (1), which is described elsewhere [35].

$$d = -\ln(T_s)/\mu \quad (1)$$

where, d is the solid thickness of sample, T_s is the X-ray transmission that is measured by recording the incident flux (I_0) and transmitted flux (I_{BS}) using an upstream detector and a detector inside the beamstop respectively. μ is the linear adsorption coefficient of the sample (the density of 2.0 g cm^{-3} for amorphous carbon was used for the calculation).

SAXS data were interpreted to solely originate from the dominant scatterer within the sample, which was deemed to be the electron density difference due to porosity on the micro- and meso- length scale. It should be noted that the analysis of fractal power-law regimes within the SAXS data is limited to the q-range of the data but it has been interpreted as a representation of either rough pore surfaces or pore fractals based on its dimensionality.

The normalised SAXS patterns were then processed using the Irena package for Igor Pro (WaveMetrics) [36]. The Unified model [37] was used to fit the scattering patterns as it can describe the structural features of complex systems containing multiple structural levels. The Unified equation for one structural level combines a Guinier law and a structurally limited power law [37], as shown in Eq. (1).

$$I(q) = G\exp\left(-\frac{q^2R_g^2}{3}\right) + B(q^*)^{-P}, \quad q^* = \frac{q}{[\mathrm{erf}(qR_g/\sqrt{6})]^{-3}} \quad (2)$$

where $I(q)$ is the scattering intensity, erf( ) is the error function. *G* and *B* are the prefactors from the Guinier and power law regions respectively. R_g is the radius of gyration of the scattering objects, the pores in this case, and *P* is the scattering exponent. A detailed description of the parameters can be found in ref [37]. The extracted R_g and *P* from each structural level provide information on the size and the morphology of the pores. If we assume the pores are ~~nearly~~ spherical, their radius can be calculated by $r = \sqrt{5/3}\ R_g$. The power law slope given by *P* provides information about the fractal dimension of the pores and/or their network [26,38]. Generally, for surface fractals $4 > P > 3$ and the fractal dimension $D_s = -P + 6$. A smooth surface corresponds to $D_s = 2$ and the surface roughness increases with increasing D_s. For mass or pore fractals $P < 3$ and the fractal dimensions $D_m = D_p = P$. Pore fractal can be viewed as the negative image of mass fractal. The ~~dimension of~~ pore fractal dimension (D_p) describes the space-filling and branching properties of pores in a structure [26].

The specific surface area (*S*) was calculated (Eq. 3) using the parameters extracted from the unified fit [38,39].

$$S(r) = Sr^{2-D_s} \quad (3)$$

where *r* is the size of the 'measurement stick' for which 4 Å $(\text{the size of a nitrogen molecule})$ was used, and *S* is given by:

$$S = 2\pi\varphi(1-\varphi)B/Q\rho_{bulk}F(D_s) \quad (4)$$

where *F*(*Ds*), the mass fraction φ and the high-*q* invariant *Q* are given by the following:

$$F(D_s) = \Gamma(5-D_s)\sin[\pi(3-D_s)/2]\,/(3-D_s) \quad (5)$$

$$\varphi = \rho_{bulk}/\rho_{base\ material} \quad (6)$$

$$Q = \int_0^\infty I(q)q^2 dq = 2\pi^2 G/V_p \quad (7)$$

Where ρ_{bulk} and $\rho_{base\ material}$ are the bulk density (see ref. [40] for the calculation) and the primary particle density (2.0 g cm^{-3}) of sample, V_p is the volume of the primary particles (pores in our case).

The pore size distribution was determined using the IPG/TNNLS (Internal Point Gradient-Total Non-Negative Least Square) fitting method in Irena [36]. This model provides a size distribution assuming a dilute dispersion of scattering features, but has been verified to provide accurate size distributions even for scattering features that demonstrate fractal aggregation [41].

3. Results and discussion

3.1. Pore development of biochar gasification at 800 °C in H_2O, CO_2 and H_2O/CO_2.

3.1.1. *In situ* SAXS patterns of biochar during gasification

Fig. 2 shows the SAXS patterns of biochar during gasification for 60 min at 800 °C in (a) H_2O, (b) CO_2, and (c) H_2O/CO_2 mixture. The scattering intensity $I(q)$ was plotted on log-log scale and the scattering intensities are on an absolute scale. The sequences of scattering patterns represent the changes in the scatterers (pores in our case) from the beginning of the gasification (blue line in graph) until after 60 min of reaction (red line). The intensities (I) as a function of the scattering vector (q) are due to X-rays scattered from the electron density difference between the carbon matrix and the empty pores (the scattering from the gases used in experiments is negligible) at various length scales [29]. The intensities in the high q region (roughly $q > 0.3$ Å^{-1}) correspond to the features of micropores (pore diameter less than 20 Å). Similarly, intensities in the low q region (roughly $q < 0.3$ Å^{-1}) reflect scattering from

mesopores (pore diameter between 20 and 500 Å). The increase or decrease in the scattering intensity shows the general growth or reduction of the specific surface area (SSA) and/or volume from micro- (high *q*) and mesopores (low *q*).

For all the biochars gasified (in H_2O, CO_2 or H_2O/CO_2) at 800°C, there are obvious changes in the SAXS intensities throughout the gasification process, reflecting the transformations in the pore structure over time. There is a clear increase in the intensities at low *q* as the gasification progresses, indicating that the volume fraction of mesopores steadily increases over time. There are also differences in the increase of intensities at low *q* among the three gasifying agents, indicating the differences in the mesopore development in biochar during gasification in different gasifying agents. As for the intensities at high *q*, a slight decrease is observed as the conversion proceeds. During gasification in H_2O/CO_2, the intensities at *q* higher than 0.2 $Å^{-1}$ decreased with increasing time, implying the reduction of the micropore volume. Also, the intensity decrease is more significant in H_2O/CO_2 than any in either H_2O or CO_2 alone. The reactions occuring on the size scale of the micropores appear to be enhanced by the presence of both H_2O and CO_2. The differences in the SAXS patterns among different gasifying agents show the differences in pore development in biochar gasified in different gases.

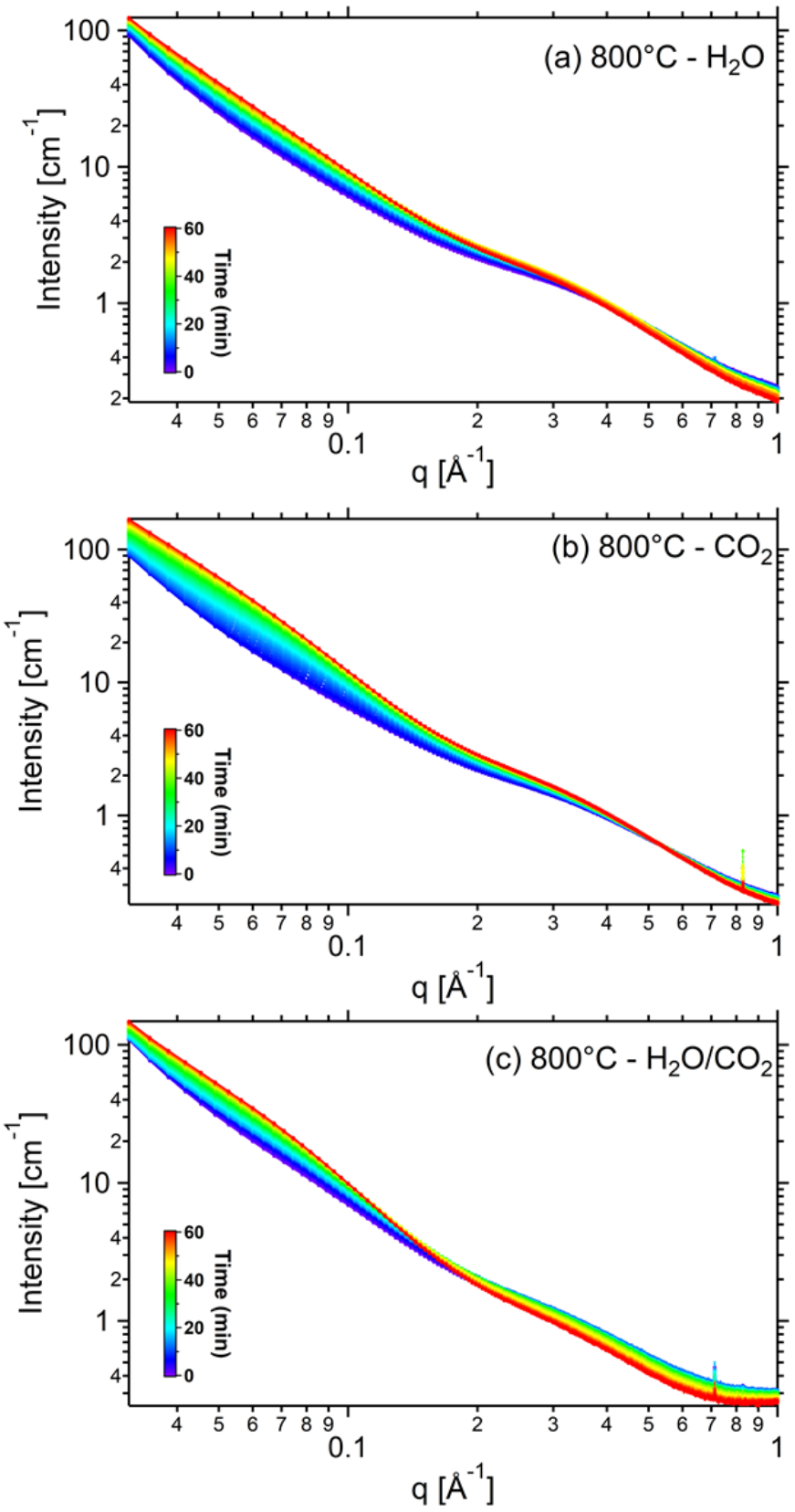

Fig. 2. Time-resolved SAXS patterns of biochar during gasification in (a) H_2O, (b) CO_2 and (c) H_2O/CO_2 at 800°C. The SAXS curves were plotted on linear time scale.

3.1.2. SAXS analysis

Before further analysis, it should be pointed out that the porosity in biochar originates from the disordered organisation of the amorphous carbon structures. The pore development of biochar during gasification is the result of the selective removal of carbon atoms by reacting with gasifying agents. During gasification, some ultramicropores (pore size is smaller than 10 Å) will be created when some carbon atoms are selectively removed by H_2O or CO_2. The initially created ultramicropores allow the next H_2O or CO_2 molecules to enter into the pore and to continue attacking the next carbon site. In this way, an abundance of micropores will be generated in the process.

In the case of gasification in the mixture of H_2O and CO_2, both of H_2O and CO_2 molecules could access the micropores initially created either by H_2O or CO_2. This is reasonable as the molecular size of H_2O (2.75 Å) and CO_2 (3.3 Å) is much smaller than the size of micropores if they are part of an open-pore (not closed-pore) network. With the continuous removal of the interior micropore walls, micropores may turn into meso- and macropores. Additionally, pore enlargement and coalescence will also occur when reactions take place on the pore walls or if the wall between pores is consumed. However, new micropores may also be created simultaneously. Therefore, the pore distribution in biochar observed at any point is the net result~~s~~ of pore generation, pore enlargement, and pore coalescence that occur simultaneously during gasification. For example, when the rate of micropore generation is slower than the rate of micropore enlargement and/or coalescence, a reduction in micropores and an increase in mesopores would occur.

To analyse better the pore development of biochar, we selected a few datasets (gasification for 0, 10, 20, 30, 40, 50 and 60 min) and performed a fit to the data using the

Unified model [37]. Two structural levels were used in this study that represent the scattering from the (1 – high q) microporous and (2 – low q) mesoporous size regimes. As shown in Fig. 3, the first structural level at high q contains a Guinier region (presenting as a hump) and a following power law region (linear on a log-log plot). The Guinier region represents the average size of micropores (d_{micro}) and the slope of the power law region at high q (not shown) gives information on the texture of micropores [37,38]. To get a stable fit to the data we had to assume that the micropore surface was smooth and thus fixed the slope of the high q power law region at 4. This is also reasonable on this length-scale (sub-20 Å) due to the limited possibilities for roughness when C-C bonds are approximately 1.5 Å. Due to the limited q range, we do not see a Guinier regime from mesopores, which would exist at even lower q. As a result, the second structural level at low q only covers a power law region (P, green line), giving fractal information from the mesopore size regime. As such, the average size of mesopores, as well as an accurate mesopore volume, is not able to be extracted from the data. Measurements covering a wider q range will be conducted in future work.

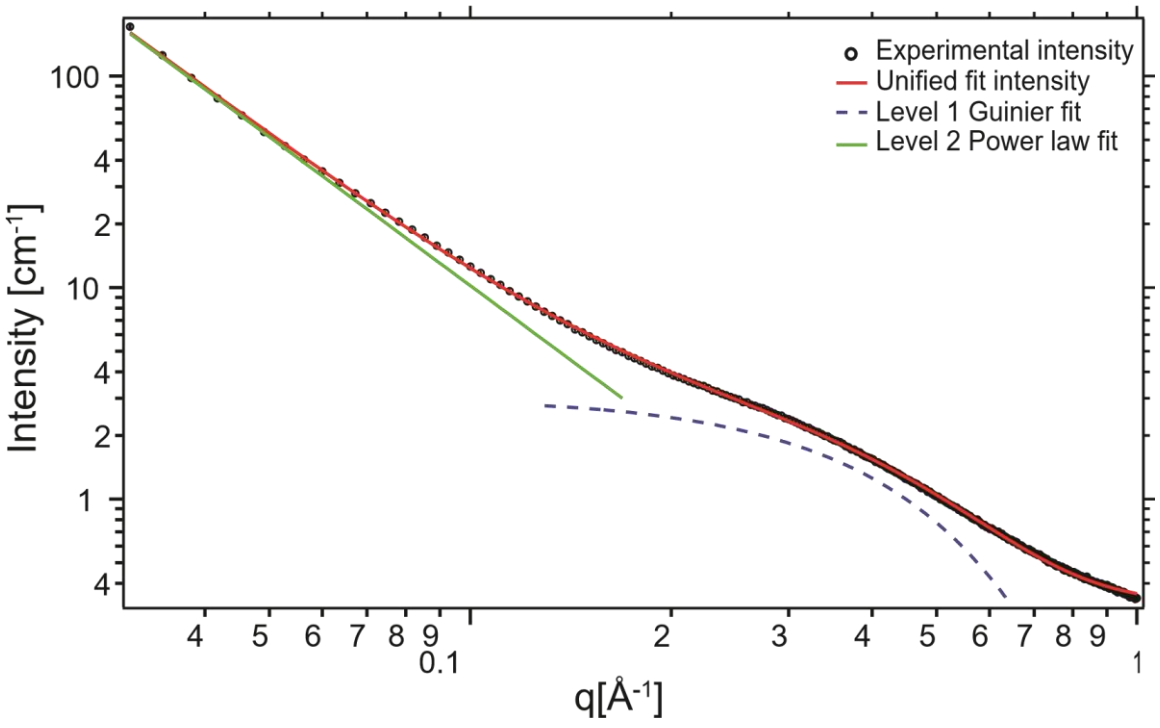

Fig. 3. A representative set of SAXS data (black circles) and a two-level unified model (red line) reproduces the experimental data.

The derived parameters from the refined unified model are shown in Table 1. The overall average diameter of micropores (d_{micro}) in the gasified biochar was calculated to be around 10 Å. Additionally, in the three data series, the average size of the micropores gradually increased over time during gasification. This demonstrates the occurrence of widening of micropores during gasification. ~~which results from the removal of micropore walls by H_2O and/or CO_2 molecules.~~ The increase in the size of micropores was more rapid with reaction time in the case of mixed gas H_2O/CO_2 gasification compared to that in the case of H_2O or CO_2 gasification. This could be due to the enhanced removal of the interior micropore walls as both H_2O and CO_2 molecules can penetrate into the micropores initially created by H_2O or CO_2.

Table 1. Derived average diameter of micropores (d_{micro}), micropore volume (V_{micro}), fractal dimension (D_p, D_s) and SSA from the two-level unified fit of SAXS patterns for biochar gasified in H_2O, CO_2 and H_2O/CO_2 at 800°C for different times (10–60 min). Note: the average diameter of micropores was calculated by assuming the pores are spherical. For surface fractal, $D_s = -P + 6$ and for pore fractal, $D_p = P$.

	0 min	10 min	20 min	30 min	40 min	50 min	60 min
H_2O							
d_{micro} (± 0.5 Å)	9.8	9.9	10.4	10.9	11.1	11.3	12.0
V_{micro} (± 0.01 cm^3/g)	0.19	0.20	0.20	0.20	0.20	0.20	0.19
Fractal dimension (± 0.05)	D_p = 2.4	D_p = 2.4	D_p = 2.7	D_p = 2.9	D_s = 3.0	D_s = 3.0	D_s = 3.1
SSA (± 1 m^2/g)	106	122	139	154	166	179	195
CO_2							
d_{micro} (± 0.5 Å)	10.1	10.5	10.6	10.7	10.8	10.9	11.0
V_{micro} (±0.01 cm^3/g)	0.18	0.20	0.21	0.21	0.21	0.21	0.22
Fractal dimension (± 0.05)	D_p = 2.4	D_p = 2.4	D_p = 2.4	D_p = 2.4	D_p = 2.5	D_p = 2.6	D_p = 2.7
SSA (± 1 m^2/g)	106	188	212	215	218	216	215
H_2O/CO_2							

d_{micro} (± 0.5 Å)	10.1	11.6	11.7	12.0	12.3	12.8	13.3
V_{micro} (±0.01 cm^3/g)	0.19	0.19	0.20	0.20	0.19	0.17	0.15
Fractal dimension (± 0.05)	D_p = 2.4	D_p = 2.5	D_p = 2.7	D_p = 2.9	D_s = 3.1	D_s = 3.3	D_s = 3.4
SSA (± 1 m^2/g)	107	127	182	205	211	232	250

When the gasification time was extended from 10 to 60 min, the micropore volume (V_{micro}) decreased slightly for the biochar gasified in H_2O and H_2O/CO_2. The decrease is more evident for biochar gasified in H_2O/CO_2. On the contrary, an insignificant increase of the micropore volume was observed in biochar gasified with CO_2. The subtle changes in the micropore volume coincide with the slight variations in the SAXS intensity at high q observed from Fig. 2. The micropore development during gasification with H_2O and H_2O/CO_2 presents a relatively constant and slightly decreased micropore volume over time, suggesting a decrease in the quantity of micropores to compensate for a larger average micropore size. The greater reduction of the micropore volume in H_2O/CO_2 gasified biochar indicates that the rate of micropore enlargement become higher than that of micropore creation at the late stage of the process. This could be attributed to the rapid removal of large amount of carbon atoms by both H_2O and CO_2 molecules, causing the rapid destruction/collapse of micropore walls. The results suggest that there could be a synergy effect between H_2O and CO_2 in attacking various active carbon sites. For example, the micropore wall left by H_2O is preferentially consumed by CO_2, consequently, a rapid enlargement of micropores would occur. Unlike gasification in H_2O and H_2O/CO_2, the rate of micropore enlargement is probably slower than that of new micropore generation for CO_2 gasification. Consequently, within the experimental time in this study, there is a steady increase in the micropore volume of the CO_2 gasified biochar.

The pore sizes and volume fractions derived from the Unified fit (as reflected in Table 1) are comparable to the pore size distribution obtained using the IPG/TNNLS fitting method in Irena [36], as shown in Fig. 4. Similarly, most of the micropores are around 10 Å and no obvious changes in the pore volume distribution is observed. If we compare the micropore volume for biochar gasified in different atmospheres for the same time, the biochar gasified in CO_2 has the highest micropore volume, followed by the biochar gasified in H_2O, whilst the micropore volume in biochar gasified in H_2O/CO_2 is the lowest. This agrees with literature [5,6,13,15,16], where ~~they also find that~~ gasification with H_2O leads to biochar with a lower micropore volume than CO_2. ~~During H_2O and/or H_2O/CO_2 gasification,~~ It seems that the enlargement of micropores could be a primary phenomenon in the presence of H_2O. ~~converting micropores to bigger pores outside of this size regime.~~ Accordingly, the resulting in biochars exhibit a low micropore volume at the late stage of the process after gasification in H_2O and/or H_2O/CO_2.

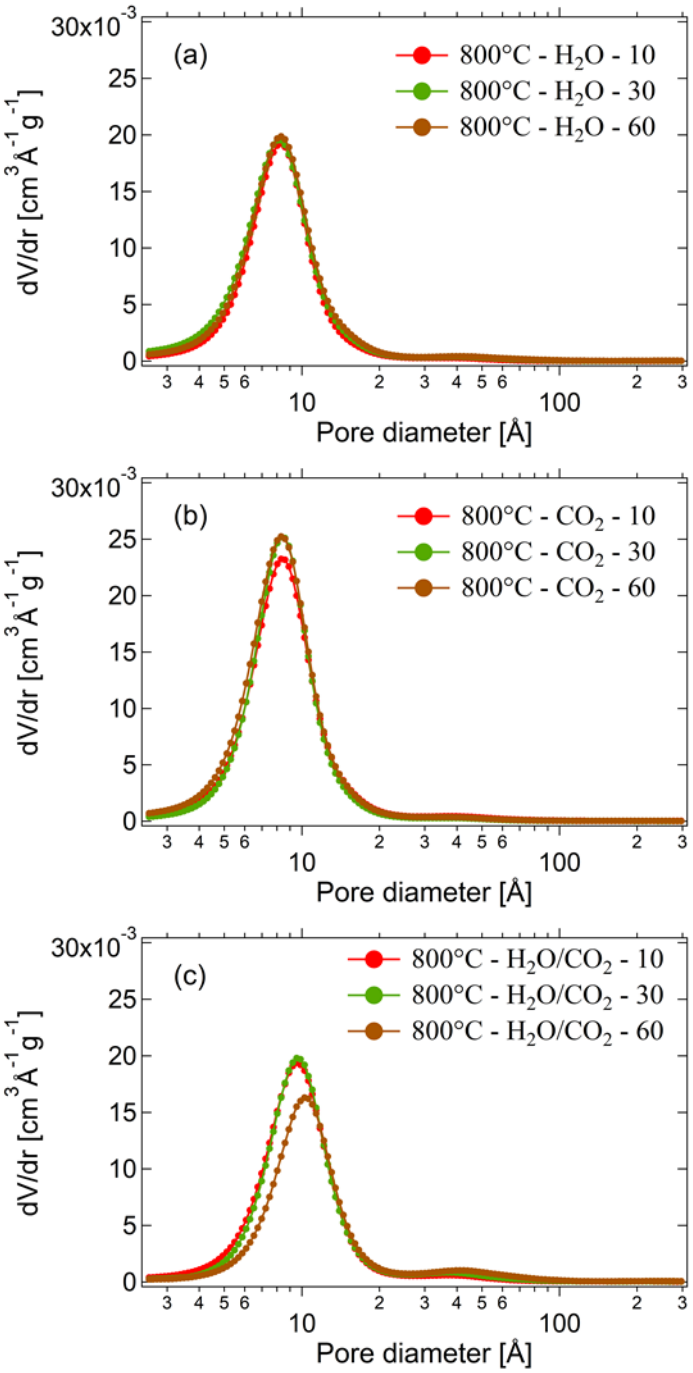

292

293 Fig. 4. Pore size and volume distribution of biochar over gasification time (10, 30 and 60

294 min) in (a) H_2O, (b) CO_2 and (c) H_2O/CO_2. The results were obtained from the IPG/TNNLS

295 fitting method to SAXS data.

296 The specific surface area (SSA, as shown in Table 1) can also be extracted from the

297 SAXS data where it can be seen that both of the H_2O and H_2O/CO_2 gasified biochars showed

298 significant growth after gasification for 60 min (60% and 97% growth respectively). The
299 biochar derived from gasification in H_2O/CO_2 has the highest SSA (250 m^2/g). However, only
300 a small increase was observed for the biochar gasified in CO_2 (14% growth). The reason for
301 the growth of SSA could be due to the rough surface of mesopores [39], which will be
302 discussed later.

303 One of the most important parameters to help understand the evolution of pore
304 structure in biochar is the fractal information of the pore network, which is a measure of its
305 morphology. Fractal information is an intrinsic characteristic of an object, regardless of the
306 scale at which it is viewed [24,38]. This fractal property can be used to describe the surface
307 roughness of a pore (surface fractal) or the aggregation of a network of smaller pores (pore
308 fractal) [26]. The modelled fractal dimensions of mesopores from SAXS data are presented in
309 Table 1. As mentioned above, the power law slope (*P*) lies between 1 and 3 for pore fractals
310 and between 3 and 4 in the case of surface fractals. In this scenario, a pore fractal where P
311 approaches 2 describes an almost sheet-like network (do not display branching), and
312 conversely when P approaches 3, the fractal dimension describes an extremely disordered
313 pore network in three dimensions that is akin to a sponge-like morphology. The power law
314 slope *P* in the surface fractal regime approaches 3 for an extremely rough surface, bordering
315 on becoming a sponge-like aggregate of pores/surface. Whereas, when a power law slope *P*
316 becomes 4 it is a representation of a perfectly smooth surface.

317 For the biochar gasified in CO_2, the *P* values suggest a pore fractal of dimension D_p =
318 2.4 where the dimension increases (to 2.7) as gasification proceeds. The results indicate that
319 micropores are distributed across biochar in a way that forms a network of micropore clusters
320 of a particular size that become more sponge-like and more branched over time. At the end

of gasification, the derived biochar presents a porous network of clusters of branched micropore aggregates [26,42]. As mentioned before, the way in which the pore network of biochar evolves reflects the way in which the carbon atoms are removed. The evolution of the fractal features in biochar during CO_2 gasification suggests that the removal of carbon atoms occurs in clusters at particular locations. CO_2 molecules react with carbon atoms at particular active sites, inducing the local etching of pore walls to form mesoporous channels of uniform size. This process then branches in a new direction in such a way that the remaining carbon solid is riddled with micropore clusters, leaving behind a porous network with a fractal dimension just below 3.

In contrast, the pore evolution during gasification in H_2O and H_2O/CO_2 occurs differently to that in CO_2 alone. The mesopore network does exhibit a branched and disordered pore network (pore fractal) at the early stages of gasification but the pore network transitions into a surface fractal at the late stage, representing a larger mesopore with a rough surface where the cluster of micropore channels used to reside. Essentially, this is the physical representation of the transition from a pore fractal to a surface fractal. This process is akin to removing solid material from a sponge-like object until there only remains a larger pore without many interconnected solids across that pore, but only a remnant of solid roughness on the surface of the larger pore. Thus, considerable numbers of carbon atoms are removed at the late stages of gasification, giving rise to the collapse and damage of micropore walls. As a result, a rough surface in the mesopores is detected instead of the previous branched micropore network. The different pore evolution, reflected by the fractal dimension, between H_2O and CO_2 gasified biochar could result from the different reactivity of H_2O and CO_2 with carbon [5,10,43]. At 800°C, lower energy is needed to dissociate a H_2O molecule than for a CO_2 molecule (the apparent activation energies are 275 and 211 kJ/mol for CO_2 and H_2O, respectively)

[5,43,44]. The high reactivity of H_2O makes it less selective in reacting with biochar in comparison to CO_2. Therefore, H_2O molecules react with carbon atoms located almost anywhere. Carbon atoms can be removed layer after layer to essentially carve out a mesopore from a cluster of smaller micropores. With the continuous elimination of carbon atoms in this way, the pore network transits from a pore fractal to surface fractal. This could also be a principal process during the gasification in H_2O/CO_2, giving rise to the similar changes in fractal dimensions of biochar to that of H_2O gasified biochar. The high selectivity of CO_2 results in preferred carbon attack, and thus the development of a more branched micropore network.

Our *in situ* SAXS data has shown clear differences in pore development especially the fractal properties between biochar gasified in H_2O and CO_2. The fractal feature of the porous network in biochar shows the way in which pores (empty phase) distribute in the two-phase structure. Thus, from another perspective, it also reflects the way of the arrangement and organisation of the carbon matrix (solid phase). Therefore, the different fractal features of biochar gasified in H_2O and CO_2 has further confirmed that the reaction pathway for biochar gasification in H_2O is different from that in CO_2 [45,46]. Pore enlargement is a prominent phenomenon during gasification in H_2O and H_2O/CO_2, while CO_2 tends to produce biochar with a high micropore volume in a branched network. A significant increase in SSA of biochar was observed during gasification in H_2O and H_2O/CO_2, which is predominantly associated with the development of rough mesopore surfaces. The simultaneous use of H_2O and CO_2 produced a higher SSA in biochar than the case in which only H_2O or CO_2 was used, due to a synergistic development of rough surfaced mesopores and additional branched micropore clusters. ~~The biochar derived from CO_2 gasification presents purely as a pore fractal. However, a transition from pore fractal to surface fractal was observed for the biochar gasified in H_2O~~

~~and H_2O/CO_2.~~ The result is generally consistent with the findings obtained using gas adsorption techniques and SAXS by others [5,6,11,13,15,16,47].

3.2. The impact of temperature on pore development of biochar during gasification in H_2O and/or CO_2.

3.2.1. Pore development during gasification at 700°C in H_2O and CO_2.

Fig. 5 shows the SAXS patterns of biochar during (a) H_2O gasification at 700°C and (b) CO_2 gasification at 700°C for 60 min. As expected, unlike gasification at 800°C, only minor changes in the intensities were shown when biochar was gasified at 700°C. This is particularly true for the case of gasification in CO_2 (Fig. 5b), during which the SAXS patterns barely changed. The data imply that the pore structure of biochar changed slightly or stayed almost unchanged. This is because, at 700°C, the reactions were modest and unable to eliminate sufficient carbon atoms to cause porosity development.

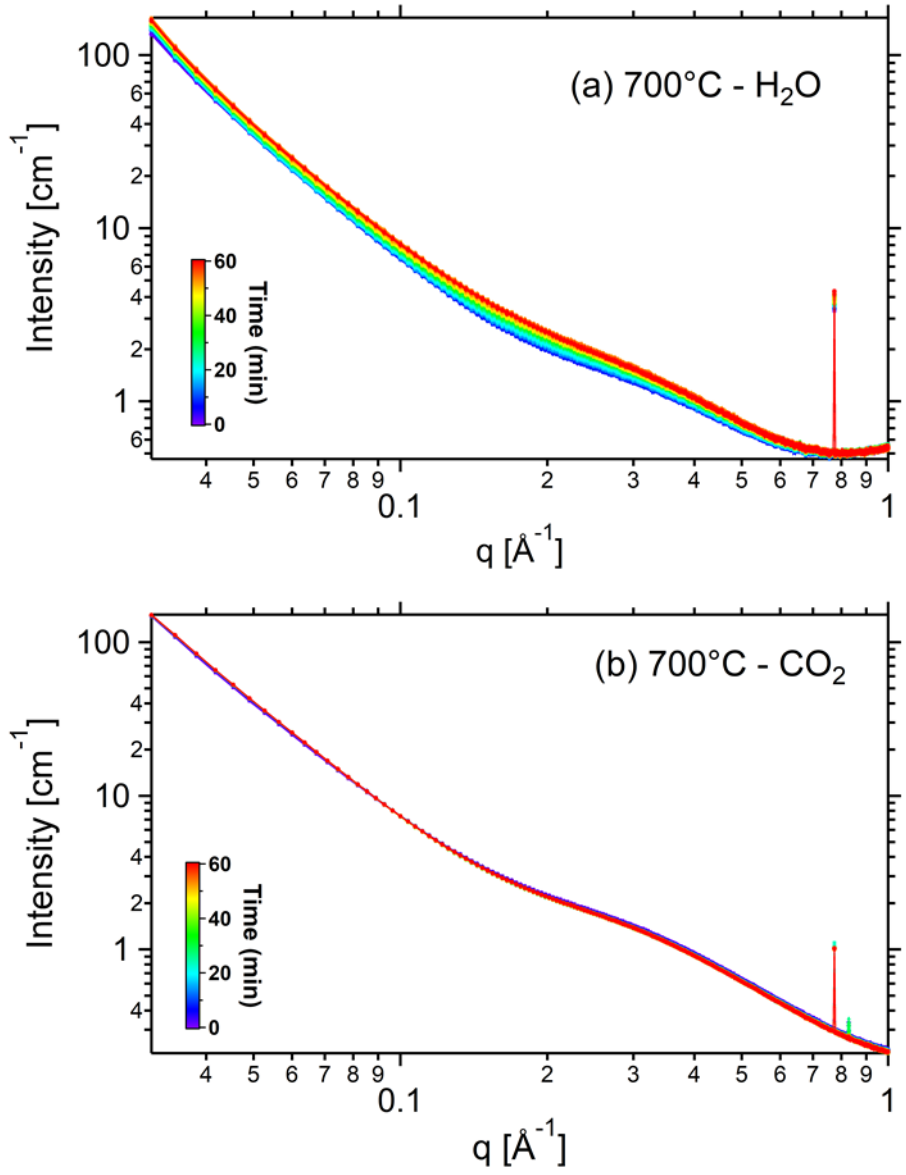

Fig. 5. SAXS patterns of biochar during gasification at 700°C (a) in H_2O for 60 min, (b) in CO_2 for 60 min. Please be noted that the peaks at high q ~~is~~ from the detector and can be neglected.

Despite the small changes in the scattering intensities, the SAXS patterns of biochar changed more significantly during gasification in H_2O than that during CO_2 gasification. The SAXS intensities showed a slightly increasing trend in intensities for the whole *q* range over the 60 min of gasification in H_2O, suggesting the development of both micropores and mesopores or the increase of SSA in biochar. The barely visible changes in SAXS patterns of CO_2 gasified biochar is most likely ascribed to the lower reactivity of CO_2 compared to H_2O

393 [5,44,48]. At 700°C, the reactivity of carbon sites with CO_2 is not high enough for intense
394 reactions to take place. For this reason, the pore structure of biochar is nearly constant
395 throughout the process [22].

396

397 3.2.2. Pore development during gasification at 900°C in H_2O.

398

399 As gasification is typically carried out between 800 and 900°C, it is of more practical
400 significance to investigate the pore development of biochar at temperatures above 800°C.
401 Thus we also performed the gasification in H_2O at 900°C. It is worth mentioning that the
402 measurement was ceased after 35 min of gasification when the biochar was completely
403 consumed. The quick conversion of biochar is due to the enhanced thermal cracking and
404 gasification reactions at 900°C. The SAXS patterns of biochar are displayed in Fig. 6. Before
405 the completion of reactions, the evolution of scattering intensity (Fig. 6b) is similar to that
406 obtained for biochar during gasification in H_2O at 800°C (Fig. 2a). When the reaction went to
407 completion, the total intensity dropped quickly and eventually was shown as the red line in
408 Fig. 6a. It can be seen that the signals at high q disappeared eventually, demonstrating a
409 complete loss of microporosity. The scattering intensity at low q shows a q^{-4} dependency (P =
410 4), as indicated by the black line in Fig. 6a, which means the scattering was generated from
411 residual bulk surface scattering.

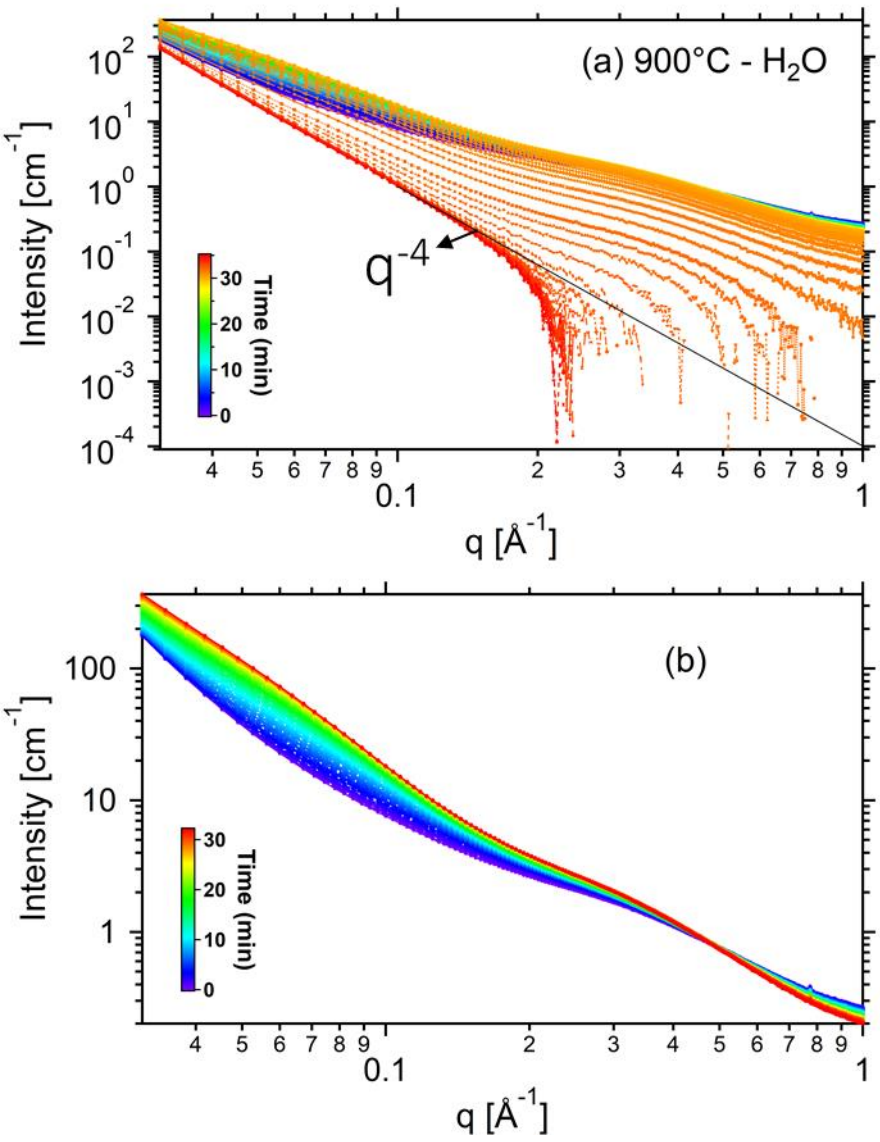

412

413 Fig. 6. (a) SAXS pattern of biochar during gasification in H_2O at 900°C until the complete
414 conversion of biochar; (b) SAXS pattern of biochar during gasification at 900°C before the
415 completion of reaction.

416 To have a better understanding of the temperature influence on pore development,
417 the pore size distributions for biochar were compared further in Fig. 7. After 30 min of
418 gasification, the increase in temperature from 700 to 800°C leads to a wider pore size
419 distribution with the growth of both micropore and mesopore volume. The rise of
420 temperature can not only promote the creation but also the enlargement of micropores. As

421 stated before, the pore development in biochar is the result of the selective removal of carbon
422 structures, which is determined by the reactivity between carbon sites and gasifying agents.
423 There are different carbon sites with various structural features and energy levels in biochar.
424 Therefore, different activation energies are required for those carbon sites to react with
425 gasifying agents. At 700°C, most of the carbon sites are not reactive enough to react with
426 gasifying agents and therefore to be removed. As a result, no obvious creation of pores will
427 be observed. When the temperature increases to 800°C, more carbon sites become reactive
428 enough to react with gasifying agents. Accordingly, an obvious development of micro- and
429 mesopores will occur, as we observed here.

430 A further rise in temperature from 800 to 900°C gives rise to a decrease in the
431 micropore volume as well as a shift of the distribution of pores to larger sizes. This is because
432 a large amount of micropores are already converted to mesopores and macropores after
433 gasification at 900°C for such a long time. During gasification at 800°C, those carbon sites with
434 lower activation energies would be gasified/consumed more easily than those with higher
435 activation energies. At 900°C, the reaction rate of carbon sites with higher activation energies
436 increases more rapidly than that of carbon sites with lower activation energies. When
437 different carbon sites have closer gasification rates, carbon removal become less selective
438 and a less significant micropore creation would occur at 900°C. Pore development would be
439 dominated by the development of large pores due to the enhanced gasification rate and
440 thermal cracking. Therefore, at a similar biochar conversion level (after gasification at 900°C
441 for 10 min and at 800 for 30 min, see ref [49]), the biochar gasified at 900°C has a lower
442 micropore volume (0.12 cm^3/g) than the biochar gasified at 800°C (0.20 cm^3/g).

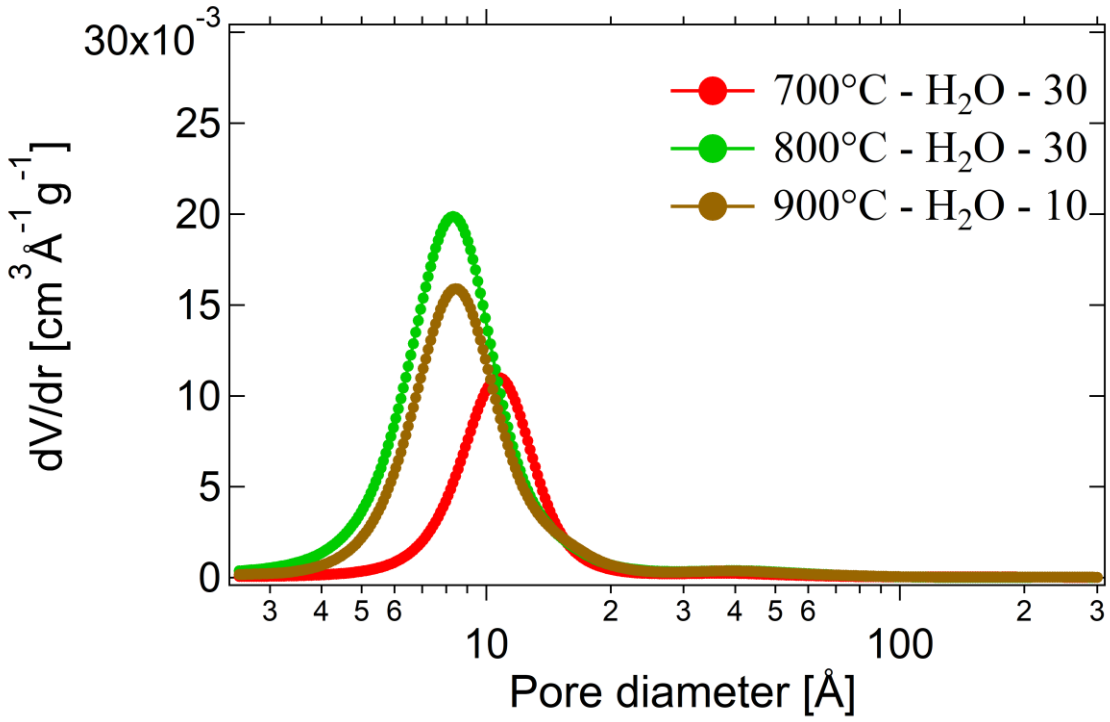

443

444 Fig. 7. Pore size and volume distribution for biochars after 30 min gasification in H_2O at 700

445 and 800°C, 10 min at 900°C.

446

447 ## 4. Conclusion

448

449 The evolution in pore structure of biochar during gasification was investigated *in situ*

450 using synchrotron SAXS. Differences in the pore development were observed for biochar

451 gasified in different atmospheres (H_2O, CO_2, and H_2O/CO_2) and at different temperatures (700,

452 800 and 900°C). H_2O started to create micro- and mesopores at 700°C while the pore structure

453 of biochar stayed nearly unchanged during CO_2 gasification at 700°C. At 800°C, the

454 simultaneous use of H_2O and CO_2 led to a higher SSA in biochar than the case in which only

455 H_2O or CO_2 was used. The CO_2 gasified biochar exhibited a high micropore volume while the

456 enlargement of micropores was a pronounced phenomenon during H_2O and H_2O/CO_2

457 gasification. Moreover, the mesoporous network of biochar gasified in CO_2 presented pore
458 fractal features throughout the whole gasification process. A transition from pore fractal to
459 surface fractal was observed for the biochar gasified in H_2O and H_2O/CO_2. The differences in
460 the evolution of pore structure between biochar gasified in H_2O and CO_2 could be attributed
461 to the different reactivity of H_2O and CO_2. CO_2 is less reactive and more selective towards
462 reacting with biochar. It was found that the increase in temperature enhanced reaction rates
463 and makes carbon removal less selective, leading to the enhanced rate of pore creation and
464 enlargement.

465

466 Acknowledgement

467

468 The authors acknowledge the financial support from the Australian Research Council
469 (DP180101788, FT160100303). This project also received funding from the Australian
470 Government through ARENA's Emerging Renewables Program. This research was undertaken
471 on the SAXS beamline at the Australian Synchrotron, part of ANSTO.

472

473 Reference

474

475 [1] C.-Z. Li, Special issue—gasification: a route to clean energy, Process Saf. Environ. Prot.
476 84 (2006) 407–408. https://doi.org/10.1205/psep.ed.0606.

477 [2] C.-Z. Li, Importance of volatile-char interactions during the pyrolysis and gasification
478 of low-rank fuels - A review, Fuel. 112 (2013) 609–623.
479 https://doi.org/10.1016/j.fuel.2013.01.031.

[3] S. Wang, L. Wu, X. Hu, L. Zhang, K.M. O'Donnell, C.E. Buckley, C.-Z. Li, An X-ray photoelectron spectroscopic perspective for the evolution of O-containing structures in char during gasification, Fuel Process. Technol. 172 (2018) 209–215. https://doi.org/10.1016/j.fuproc.2017.12.019.

[4] H. Wu, K. Yip, F. Tian, Z. Xie, C.-Z. Li, Evolution of char structure during the steam gasification of biochars produced from the pyrolysis of various mallee biomass components, Ind. Eng. Chem. Res. 48 (2009) 10431–10438. https://doi.org/10.1021/ie901025d.

[5] F. Rodríguez-Reinoso, M. Molina-Sabio, M.T. González, The use of steam and CO_2 as activating agents in the preparation of activated carbons, Carbon N. Y. 33 (1995) 15–23. https://doi.org/10.1016/0008-6223(94)00100-E.

[6] J. Pastor-Villegas, C.J. Durán-Valle, Pore structure of activated carbons prepared by carbon dioxide and steam activation at different temperatures from extracted rockrose, Carbon N. Y. 40 (2002) 397–402. https://doi.org/10.1016/S0008-6223(01)00118-X.

[7] Y. Liu, M. Paskevicius, H. Wang, G. Parkinson, J.P. Veder, X. Hu, C.-Z. Li, Role of O-containing functional groups in biochar during the catalytic steam reforming of tar using the biochar as a catalyst, Fuel. 253 (2019) 441–448. https://doi.org/10.1016/j.fuel.2019.05.037.

[8] Y. Liu, M. Paskevicius, H. Wang, C. Fushimi, G. Parkinson, C.-Z. Li, Difference in tar reforming activities between biochar catalysts activated in H_2O and CO_2, Fuel. 271 (2020) 117636. https://doi.org/10.1016/j.fuel.2020.117636.

[9] K. Tomków, T. Siemieniewska, F. Czechowski, A. Jankowska, Formation of porous structures in activated brown-coal chars using O_2, CO_2 and H_2O as activating agents, Fuel. 56 (1977) 121–124. https://doi.org/10.1016/0016-2361(77)90129-6.

[10] J.F. González, J.M. Encinar, C.M. González-García, E. Sabio, A. Ramiro, J.L. Canito, J. Gañán, Preparation of activated carbons from used tyres by gasification with steam and carbon dioxide, Appl. Surf. Sci. 252 (2006) 5999–6004. https://doi.org/10.1016/j.apsusc.2005.11.029.

[11] G.H. Coetzee, R. Sakurovs, H.W.J.P.J.P. Neomagus, L. Morpeth, R.C. Everson, J.P. Mathews, J.R. Bunt, Pore development during gasification of South African inertinite-rich chars evaluated using small angle X-ray scattering, Carbon N. Y. 95 (2015) 250–260. https://doi.org/10.1016/j.carbon.2015.08.030.

[12] I. Sircar, A. Sane, W. Wang, J.P. Gore, Experimental and modeling study of pinewood char gasification with CO_2, Fuel. 119 (2014) 38–46. https://doi.org/10.1016/j.fuel.2013.11.026.

[13] M. Molina-Sabio, M.T. González, F. Rodriguez-Reinoso, A. Sepúlveda-Escribano, Effect of steam and carbon dioxide activation in the micropore size distribution of activated carbon, Carbon N. Y. 34 (1996) 505–509. https://doi.org/10.1016/0008-6223(96)00006-1.

[14] F. Rodríguez-Reinoso, Controlled gasification of carbon and pore structure development, in: E.P. Lahaye J. (Ed.), Fundam. Issues Control Carbon Gasif. React., Springer, Dordrecht, 1991: pp. 533–571. https://doi.org/10.1007/978-94-011-3310-4_26.

[15] J. Gonzalez, J.F. Gonza, S. Roma, C.M. Gonza, A.L. Ortiz, R. Roma, Porosity Development in Activated Carbons Prepared from Walnut Shells by Carbon Dioxide or Steam Activation Porosity Development in Activated Carbons Prepared from Walnut Shells by Carbon Dioxide or Steam Activation, (2009) 7474–7481. https://doi.org/10.1021/ie801848x.

[16] Y. Bai, P. Lv, X. Yang, M. Gao, S. Zhu, L. Yan, F. Li, Gasification of coal char in H_2O/CO_2 atmospheres: Evolution of surface morphology and pore structure, Fuel. 218 (2018) 236–246. https://doi.org/10.1016/j.fuel.2017.11.105.

[17] M. Kalliat, C.Y. Kwak, P.W. Schmidt, B.E. Cutter, E.A. McGinnes, Small angle X-ray scattering measurement of porosity in wood following pyrolysis, Wood Sci. Technol. 17 (1983) 241–257. https://doi.org/10.1007/BF00349913.

[18] M. Foster, K.F. Jensen, Small angle X-ray scattering investigations of pore structure changes during coal gasif ication, 69 (1990) 88–96.

[19] M.H. Reich, S.P. Russo, I.K. Snook, H.K. Wagenfeld, The application of SAXS to determine the fractal properties of porous carbon-based materials, J. Colloid Interface Sci. 135 (1990) 353–362. https://doi.org/10.1016/0021-9797(90)90005-9.

[20] M.D. Foster, K.F. Jensen, SAXS investigation of model carbon pore structure and its change with gasification, Carbon N. Y. 29 (1991) 271–282. https://doi.org/10.1016/0008-6223(91)90077-V.

[21] T. Nakagawa, I. Komaki, M. Sakawa, K. Nishikawa, Small angle X-ray scattering study on change of fractal property of Witbank coal with heat treatment, Fuel. 79 (2000) 1341–1346. https://doi.org/10.1016/S0016-2361(99)00269-0.

546 [22] A.J. Smith, M.J. MacDonald, L.D. Ellis, M.N. Obrovac, J.R. Dahn, A small angle X-ray
547 scattering and electrochemical study of the decomposition of wood during pyrolysis,
548 Carbon N. Y. 50 (2012) 3717–3723. https://doi.org/10.1016/j.carbon.2012.03.045.

549 [23] G.N. Okolo, R.C. Everson, H.W.J.P. Neomagus, M.J. Roberts, R. Sakurovs, Comparing
550 the porosity and surface areas of coal as measured by gas adsorption, mercury
551 intrusion and SAXS techniques, Fuel. 141 (2015) 293–304.
552 https://doi.org/10.1016/j.fuel.2014.10.046.

553 [24] G. Beaucage, Determination of branch fraction and minimum dimension of mass-
554 fractal aggregates, Phys. Rev. E - Stat. Physics, Plasmas, Fluids, Relat. Interdiscip. Top.
555 70 (2004) 10. https://doi.org/10.1103/PhysRevE.70.031401.

556 [25] P. Pfeifer, Fractal dimension as working tool for surface-roughness problems, Appl.
557 Surf. Sci. 18 (1984) 146–164. https://doi.org/10.1016/0378-5963(84)90042-4.

558 [26] P. Pfeifer, F. Ehrburger-Dolle, T.P. Rieker, M.T. González, W.P. Hoffman, M. Molina-
559 Sabio, F. Rodríguez-Reinoso, P.W. Schmidt, D.J. Voss, Nearly space-filling fractal
560 networks of carbon nanopores, Phys. Rev. Lett. 88 (2002) 115502.
561 https://doi.org/10.1103/PhysRevLett.88.115502.

562 [27] H.D. Bale, P.W. Schmidt, Small-Angle X-Ray-Scattering Investigation of
563 Submicroscopic Porosity with Fractal Properties, Phys. Rev. Lett. 53 (1984) 596–599.
564 https://doi.org/10.1103/PhysRevLett.53.596.

565 [28] N.M. Kirby, S.T. Mudie, A.M. Hawley, D.J. Cookson, H.D.T. Mertens, N. Cowieson, V.
566 Samardzic-Boban, A low-background-intensity focusing small-angle X-ray scattering
567 undulator beamline, J. Appl. Crystallogr. 46 (2013) 1670–1680.

https://doi.org/10.1107/S002188981302774X.

[29] O. Glatter, O. Kratky, Small angle x-ray scattering, 1982. https://doi.org/10.1007/978-3-642-03307-0.

[30] C.A. Dreiss, K.S. Jack, A.P. Parker, On the absolute calibration of bench-top small-angle X-ray scattering instruments: A comparison of different standard methods, J. Appl. Crystallogr. 39 (2006) 32–38. https://doi.org/10.1107/S0021889805033091.

[31] Advanced biomass gasification technology, Australian Renewable Energy Agency, https://arena.gov.au/projects/advanced-biomass-gasification-technology/ (accessed May 20, 2020).

[32] Grinding pyrolysis, Renergi Pty Ltd. http://www.renergi.net/grinding_pyrolysis. (accessed October 28, 2019).

[33] A.J. Allen, F. Zhang, R. Joseph Kline, W.F. Guthrie, J. Ilavsky, NIST Standard Reference Material 3600: Absolute Intensity Calibration Standard for Small-Angle X-ray Scattering, J. Appl. Crystallogr. 50 (2017) 462–474. https://doi.org/10.1107/S1600576717001972.

[34] SAXS Software - scatterBrain, http://archive.synchrotron.org.au/aussyncbeamlines (accessed August 27, 2019).

[35] O. Spalla, S. Lyonnard, F. Testard, Analysis of the small-angle intensity scattered by a porous and granular medium, J. Appl. Crystallogr. 36 (2003) 338–347. https://doi.org/10.1107/S0021889803002279.

[36] J. Ilavsky, P.R. Jemian, Irena : tool suite for modeling and analysis of small-angle scattering, J. Appl. Crystallogr. 42 (2009) 347–353.

https://doi.org/10.1107/S0021889809002222.

[37] G. Beaucage, Approximations leading to a unified exponential power-law approach to small-angle scattering, J. Appl. Crystallogr. 28 (1995) 717–728. https://doi.org/Doi 10.1107/S0021889895005292.

[38] G. Beaucage, IUCr, Small-Angle Scattering from Polymeric Mass Fractals of Arbitrary Mass-Fractal Dimension, J. Appl. Crystallogr. 29 (1996) 134–146. https://doi.org/10.1107/S0021889895011605.

[39] A.J. Hurd, D.W. Schaefer, D.M. Smith, S.B. Ross, A. Le Méhauté, S. Spooner, Surface areas of fractally rough particles studied by scattering, Phys. Rev. B. 39 (1989) 9742–9745. https://doi.org/10.1103/PhysRevB.39.9742.

[40] M. Paskevicius, A nanostructural investigation of mechanochemically synthesised hydrogen storage materials (thesis), 2009.

[41] G. Beaucage, H.K. Kammler, S.E. Pratsinis, Particle size distributions from small-angle scattering using global scattering functions, J. Appl. Crystallogr. 37 (2004) 523–535. https://doi.org/10.1107/S0021889804008969.

[42] D. Avnir, D. Farin, P. Pfeifer, Surface geometric irregularity of particulate materials: The fractal approach, J. Colloid Interface Sci. 103 (1985) 112–123. https://doi.org/10.1016/0021-9797(85)90082-7.

[43] J.F. González, S. Román, C.M. González-García, J.M.V. Nabais, A.L. Ortiz, Porosity development in activated carbons prepared from walnut shells by carbon dioxide or steam activation, Ind. Eng. Chem. Res. 48 (2009) 9354. https://doi.org/10.1021/ie9013293.

[44] S. Román, J.F. González, C.M. González-García, F. Zamora, Control of pore development during CO_2 and steam activation of olive stones, Fuel Process. Technol. 89 (2008) 715–720. https://doi.org/10.1016/j.fuproc.2007.12.015.

[45] H.L. Tay, S. Kajitani, S. Zhang, C.-Z. Li, Effects of gasifying agent on the evolution of char structure during the gasification of Victorian brown coal, Fuel. 103 (2013) 22–28. https://doi.org/10.1016/j.fuel.2011.02.044.

[46] S. Wang, L. Wu, X. Hu, L. Zhang, T. Li, C.-Z. Li, Effects of the particle size and gasification atmosphere on the changes in the char structure during the gasification of mallee biomass, Energy and Fuels. 32 (2018) 7678–7684. https://doi.org/10.1021/acs.energyfuels.8b01309.

[47] E. Arenas, F. Chejne, The effect of the activating agent and temperature on the porosity development of physically activated coal chars, Carbon N. Y. 42 (2004) 2451–2455. https://doi.org/10.1016/j.carbon.2004.04.041.

[48] J. Pallarés, A. González-Cencerrado, I. Arauzo, Production and characterization of activated carbon from barley straw by physical activation with carbon dioxide and steam, Biomass and Bioenergy. 115 (2018) 64–73. https://doi.org/10.1016/j.biombioe.2018.04.015.

[49] S. Wang, Evolution of Char Structure and Reactivity during Gasification (thesis), Curtin University, 2016.